AIAA JOURNAL
Vol. 40, No. 5, May 2002

Temporal Turbulent Flow Structure for Supersonic Rough-Wall Boundary Layers

Robert M. Latin*
U.S. Air Force Office of Scientific Research, Arlington, Virginia 22203
and
Rodney D. W. Bowersox†
University of Alabama, Tuscaloosa, Alabama 35487

An experimental study of the temporal turbulent flow structure for high-speed ($M = 2.8$), high-Reynolds-number ($Re/m = 1.9 \times 10^7$), rough-wall boundary-layer flow was performed. Six wall topologies consisting of a smooth and five rough surfaces ($k_s^+ = 104$–571) were studied. The hot-film measurements consisted of mass-flux power spectra, autocorrelations, cross correlations, integral timescales, and flow structure angle information at three locations ($y/\delta_M = 0.25, 0.50,$ and 0.75) within the boundary layers. The power spectra curves, with inner scaling, were found to shift up and to the right with increasing roughness height at all three boundary-layer locations signifying increased turbulence production and transport. The integral scales decreased with roughness height across the boundary layers, and, for $k_s^+ \geq 250$, were nominally independent of boundary-layer location. The measurements confirmed the inertial subrange indicating that the expected cascade and dissipation mechanisms were present.

Nomenclature

A_B	=	roughness blockage area
f	=	frequency
k	=	roughness height
k_s	=	equivalent sand grain roughness height
k_1	=	wave number, $2\pi f/u$
$\bar{k}$	=	mean roughness height
M	=	Mach number
Re	=	Reynolds number
t	=	time
u	=	mean axial velocity
u_c	=	convention velocity
u'	=	Reynolds turbulent velocity fluctuation
u^*	=	friction velocity, $(\tau_w/\rho_w^{1/2})$
V	=	voltage
V'	=	fluctuating voltage
w	=	parallel film probe sensor separation distance
x, y, z	=	Cartesian coordinates
Δ	=	mean component difference operator
δ	=	velocity boundary-layer thickness (99%)
δ_M	=	Mach number boundary-layer thickness (99%)
θ	=	momentum thickness or flow structure angle
Λ	=	integral length scale
λ	=	roughness wavelength
ρ	=	mean density
ρ_ω	=	wall density
$(\rho u)'$	=	Reynolds turbulent mass flux fluctuation
σ_k	=	roughness height standard deviation
τ	=	time step
τ_ω	=	wall shear stress

Superscript

$+$	=	$\rho_w u^*(\,)/\mu_w$

Received 14 April 2001; revision received 5 October 2001; accepted for publication 12 November 2001. Copyright © 2001 by the American Institute of Aeronautics and Astronautics, Inc. All rights reserved. Copies of this paper may be made for personal or internal use, on condition that the copier pay the $10.00 per-copy fee to the Copyright Clearance Center, Inc., 222 Rosewood Drive, Danvers, MA 01923; include the code 0001-1452/02 $10.00 in correspondence with the CCC.

*Program Manager, Directorate of External Programs. Member AIAA.
†Associate Professsor, Department of Aerospace Engineering and Mechanics. Senior Member AIAA.

Introduction

ACCURATE flowfield understanding and prediction ability of high-speed rough-wall turbulent boundary layers have numerous practical applications, for example, high-speed aircraft, missiles, reentry vehicles, and propulsion systems. Direct numerical simulation of high-Reynolds-number turbulent flow is currently impractical. Hence, engineers and scientists must rely on an approximate averaged form of the governing Navier–Stokes equations. For large-eddy simulation methods, a temporal filter is applied, the large-scale structures are simulated, and the influences of the small-scale structure are modeled. For the Reynolds-averaged Navier–Stokes approach, all of the turbulent temporal content is modeled. Because of the nonlinearity of the Navier–Stokes equations, both filtering and averaging introduces additional second-order correlation unknowns into the problem. Modeling these additional unknowns has proven to be a major challenge and a limiting factor in the accuracy of high-Reynolds-number numerical simulations. Empirical information is a key element in understanding the essential dynamics and, thus, has provided the basis for current turbulence models for both low- and high-speed flows.[1–3] For low-speed rough-wall flow, the influence of surface roughness on the mean and turbulent flow properties is well documented.[1,4–7]

Raupach et al.[6] provide a comprehensive survey (157 papers) of available low-speed mean and turbulent flow scaling for laboratory- and atmospheric-scale flowfields. They extended the Reynolds number similarity concept of Townsend[8] to include rough walls by defining wall similarity as the boundary-layer turbulent motions outside the roughness or viscous sublayer at high Reynolds numbers that are independent of wall roughness and viscosity, except for the role of the wall in setting the friction velocity, effective origin, and boundary-layer thickness. Hence, in addition to Reynolds number similarity, outside the roughness layer, the roughness length scales are irrelevant.[6]

Perry et al.[7] performed a detailed investigation of the turbulent flow structure for smooth- and rough-wall flat-plate boundary layers. They defined the turbulent wall region as $\nu/u^* \ll y \ll \delta$ for smooth walls and $k \ll y \ll \delta$ for rough walls. The fully turbulent region was defined as $100\nu/u^* < y < \delta$ and $2k < y < \delta$. Inner variable scaling was defined such that the turbulent energy was normalized by the friction velocity squared, and the wave number was normalized by multiplying by y, that is, $[u'(k_1 y)/u^*]^2$. Outer variable scaling was similarly defined, except that the wave number was nondimensionalized by multiplying by δ instead of y. Perry et al. demonstrated that, when plotted with inner variable scaling, the near-wall ($y/\delta < 0.1$) smooth- and rough-wall data both exhibited

two overlap regions. Overlap region I was defined as the inner variable scaled wave number range where both inner and outer flow variable scaling hold. In region I, the power spectra are proportional to k^{-1}. Overlap region II was defined as the region where both inner and Kolmogorov[9] scaling hold. In region II, the power spectra are proportional to $k^{-5/3}$. The measurements of Perry et al.[7] clearly show both overlap regions. Raupach et al.[6] indicated that the overlap regions are more pronounced at higher Reynolds numbers. Perry et al.[7] used the presence of the overlap regions to predict the velocity fluctuation variance behavior within the inner layer, that is,

$$\overline{(u'/u^*)^2} = B_1 - A_1 \ell n(y/\delta) - C/y^{+\frac{1}{2}}$$

$$\overline{(v'/u^*)^2} = B_2 - A_2 \ell n(y/\delta) - \left(\tfrac{4}{3}\right) C/y^{+\frac{1}{2}}$$

$$\overline{(w'/u^*)^2} = A_3 \ell n(y/\delta) - \left(\tfrac{4}{3}\right) C/y^{+\frac{1}{2}}$$

where A_1, A_2, A_3, B_1, B_2, and C are 1.26, 0.63, 1.78, 2.01, 1.08, and 7.50, respectively. Raupach et al.[6] compared these relations with numerous laboratory and atmospheric data at $y/\delta = 0.1$ and found that the laboratory measurements agreed to within the experimental uncertainty. However, the atmospheric data were consistently 20–30% higher that predicted.

An important consequence of the wall similarity hypothesis is that the organized structures (double-roller eddy[8] or Λ vortex[6]) in the outer region of the rough-wall boundary layers should be the same as those for smooth-wall boundary layers, even though the near-wall vortex generation for smooth and rough walls are fundamentally different.[6] Smooth walls are characterized by the bursting process and rough surfaces by organized wake vortices. For most roughness types, the near-wall flow is so disturbed that the smooth-wall low-speed streaks are eradicated; however, there is evidence of a rough-wall counterpart.[6] Grass[10] performed detailed investigations of the influence of surface roughness on the turbulent structure and turbulence production. His data confirmed that the smooth-wall inrush and ejection process, typically associated with the bursting process, correlate with an extremely high contribution to the Reynolds stress and, hence, turbulence production close to the wall. The inrush and ejection process was found to be present irrespective of the surface roughness condition. Grass[10] also noted a strong interaction between the inner and outer flows.

For supersonic flow, the mean flowfield properties have been thoroughly documented.[11–14] However, high-speed rough-wall studies that included turbulence data are virtually nonexistent, for example, high-speed rough-wall studies were not included in recent compilations of available mean and turbulent flowfield information.[3,15] This void in the empirical database coupled with the numerous practical applications provided the impetus for the present research. As part of this study, Latin and Bowersox[11] presented a detailed examination of the mean and statistical turbulent flow properties across a series of zero-pressure-gradient boundary layers, with a variety of surface roughness conditions. Some similarities to the low-speed database were identified. Specifically, the mean velocity followed the incompressible pattern when scaled for compressibility, and the kinematic turbulence levels were in reasonable agreement with the low-speed database. Significant differences between the high-speed results and the low-speed database were also noted. The roughness elements extended into the supersonic portion of the boundary layer, and generated shock and expansion waves that extended through the boundary layer and into the freestream. These shock waves represent an interaction mechanism between the wall roughness and the outer region of the boundary layer, which is not present for low-speed flow. A comparison of the $y/\delta \approx 0.1$ $\overline{(u'/u^*)^2}$ and $\overline{(v'/u^*)^2}$ laser Doppler velocimetry data from Latin and Bowersox,[11] scaled for compressibility, with the Perry et al.[7] relations, indicated that the transverse smooth- and rough-wall data were 28 and 38% lower than the predictions, respectively. The axial data were 5 and 10% lower than the predictions, respectively. This departure from the expected trends coupled with the additional processes associated with the roughness-generated waves suggest that the turbulent flow structure for the supersonic turbulent boundary layer is significantly different than that for low-speed flows. The objective of this paper is to provide a characterization of the influence of roughness on high-speed, high-Reynolds-number boundary-layer temporal turbulent flow structure.

Facilities and Apparatus

Data were collected in a supersonic wind tunnel located at Wright–Patterson Air Force Base. The tunnel was a combination drawdown/blowdown facility. A 27.46-cm-long (measured from the throat), finite-radius, half-nozzle was used to produce a freestream Mach number at the nozzle exit of 2.88 with a $\pm 1.3\%$ variation across the test section.[16,17] The contoured side of the nozzle was located along the tunnel ceiling. The average axial velocity freestream turbulence intensity at the nozzle exit measured with a cross-film probe was nominally 0.8% (Refs. 16 and 17). The stagnation pressure and temperature were 0.237 MPa ($\pm 1.7\%$) and 296 K ($\pm 0.5\%$), respectively. The boundary-layer heights δ, δ_M, and θ at the nozzle exit were calculated from the velocity profile measured with the pitot probe as 4.7, 5.3, and 0.2 mm, respectively.[16] The cross-sectional shape of the test section was square, with each side 6.35 cm in length. For the present study, the test section length, beginning at the nozzle exit, was 66.0 cm, with the measurement location at 54.0 cm downstream of the nozzle exit (Fig. 1). The coordinate system was defined such that x was positive in the freestream flow direction, measured from the nozzle exit; y was positive vertically up relative to the tunnel floor; z completed the right-hand system, and $z = 0$ was along the tunnel span centerline. The boundary-layer properties at the measurement station for all six models are included in Table 1.

Detailed two-dimensionality studies quantifying the mean and turbulent flow statistics at off center z locations have been performed for the present facility.[16,17] In summary, the mean flow properties

Table 1 Surface roughness topology and boundary-layer properties

Model	$\bar{k}$, mm	$k_{\max}$, mm	σ_k, μm	k_s^+	A_B, mm^2	M_e	ρ_w, kg/m^3	u^*, m/s	Re_θ ($\times 10^4$)	δ_M, mm
Flat	0.007	0.02	0.005	0[a]	0	2.75	0.11	26	1.6	15.4
Two dimensional	0.56	0.58	0.007	289.0	35.6	2.73	0.12	38	2.6	18.1
Three dimensional	0.56	0.58	0.007	241.0	9.1	2.73	0.12	38	2.6	17.3
80 grit	0.53	1.10	0.17	104.0	33.7	2.73	0.12	35	2.2	16.3
36 grit	0.90	1.40	0.34	395.0	57.2	2.72	0.12	40	2.9	19.2
20 grit	0.83	1.70	0.50	571.0	52.7	2.70	0.12	40	2.9	18.2

[a]Here $k_s^+ = 0$ by definition; however, $k^+ = 1.1$.

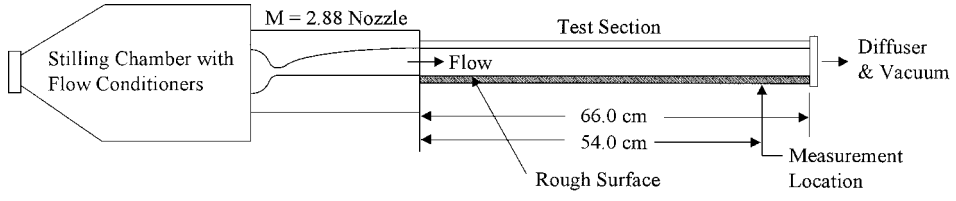

Fig. 1 Schematic of wind tunnel (not drawn to scale).

were independent of z location to within the measurement uncertainty over the center 40% of the test section (total area mapped).[16] The turbulent shear stresses at off centerline locations also agreed to within the measurement uncertainty.[17] (Total area mapped was about 20% of the test section.) The effects of the longitudinal pressure gradient due to boundary-layer growth has also been investigated,[17] and the results demonstrated that the mean and turbulent flow properties measured at x locations (in the present coordinate system with the origin at the nozzle section exit) of 16.5, 44.0, and 54.0 cm (present location) collapsed onto a single curve representative of a zero-pressure-gradient equilibrium boundary layer with outer scaling.

Six different floor sections, each with a different surface roughness, were tested. The floor sections were, as was the case for the Goddard[12] study, aligned so that the tops of the roughness elements were level with the tunnel floor at the nozzle exit (Fig. 1). Three sand-grain-roughened plates were constructed by adhering Varathane brand 80-, 36-, and 20-grit flooring sandpaper to the top surface of three aluminum flat plates ($66.0 \times 6.35 \times 1.91$ cm^3). The heights of the sand grains were not measured before being glued to the sandpaper surface. For this reason, the roughness heights of the sandpaper were not expected to correspond directly to Nikuradse sand-grain roughness. Instead, direct measurements of the roughness topography using a Carl Zeiss LSM 320 confocal laser scan microscope (LSM) were acquired. The LSM was used to provide samples of the roughness topology from which the mean, maximum, and standard deviation of the surface roughness were computed. The roughness topologies were resolved with the LSM to within 4.0% of the mean roughness height. The statistical properties from this analysis are listed in Table 1. The 20-grit plate was more sparsely populated with larger elements than the 36-grit paper. Hence, the average roughness height was smaller for the 20-grit plate. However, the maximum height and the standard deviation were largest for the 20-grit plate. These three rough surfaces were selected because they provided a relatively broad (200%) variation in the maximum heights, and all were in the fully rough regime.

Two plates with uniform roughness patterns machined therein were designed to provide insight into the effects of topology. The geometry was arbitrarily chosen to provide a large variation in the frontal blockage area A_B (opposing the flow) and the surface area occupied by roughness elements. The machined, two-dimensional, roughness element model had rectangular lateral grooves that spanned the width of the test section, and the three-dimensional model consisted of cubical pillars (Fig. 2) aligned in straight rows in both the x and z directions. The wavelength of the roughness elements was 2.18 mm. The roughness height was chosen as 0.56 mm for both the two-dimensional and three-dimensional plates so that both were fully rough. The frontal blockage area for the two-dimensional plate was the roughness height times the width of the test section, which was 290% larger than that of the three-dimensional plate. The roughness blockage area for each plate is summarized in Table 1. The surface area occupied by the two-dimensional plate roughness elements (25.7%) was 290% larger than that for the three-dimensional plate (6.6%). The milling machine accuracy was rated at ± 22 μm (± 4.0% of the roughness element height). The k_s values listed in Table 1 were computed as described by Latin and Bowersox.[11]

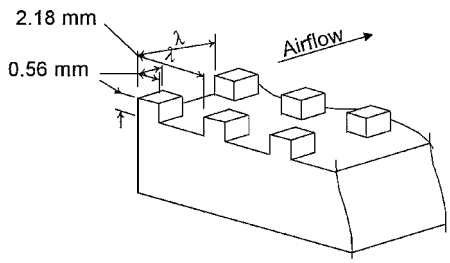

Three-dimensional plate

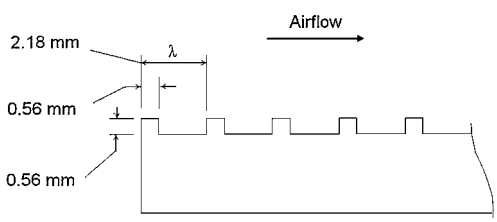

Two-dimensional plate

Fig. 2 Machined roughness patterns.

Instrumentation

Two hot-film probe types, normal and parallel, were used to collect high-frequency information in the boundary layer. The normal-film probe measured energy spectra and autocorrelation information, and the parallel-film probe measured boundary flow structure angles using the cross correlation between the two film sensors. The TSI Model 1218-20 normal-film probe had a single sensor mounted to a TSI Model 1150 single sensor probe support. The TSI Model 1246AD-20 parallel-film probe had two hot-film sensors positioned normal to the x–y plane, parallel to each other and spaced 1.085 mm apart in the y-axis direction. The parallel-film probe was mounted to a TSI Model 1155 dual sensor probe support. The sensors for both probe types had diameters of 50.8 μm, lengths of 1.02 mm, and temperature coefficients of 0.0024/°C. The present films were chosen over wires because of wire attrition in the supersonic environment. The present measurements were limited to the fully turbulent region of the boundary layer to avoid the uncertainties associated with the spatial resolution of the sensors (described later).

A DANTEC streamline constant temperature anemometry system was used to tune and maintain the bridge during the tunnel runs. For the present work, the overheat resistance ratio was set to 1.9 for all probes. The DANTEC system and external resistors provided a nominal frequency response of 100 kHz using the square wave technique in the Mach 2.9 freestream. Latin and Bowersox[11] demonstrated that the present sensors were sufficient to resolve the turbulent statistical flow properties. Furthermore, as is discussed in the "Results and Discussion" section, the present sensors resolved the spectra into overlap region II. A Nicolet Multipro 12-bit data acquisition system was used to collect hot-film voltage data. The Nicolet Multipro system consisted of a chassis unit with four A/D acquisition boards, each with four input channels. The Multipro system acquired each channel at a 1.0-MHz rate (noninterlaced) with a maximum of 256,000 samples per board.

Data Reduction

The high-frequency data collected by the DANTEC Streamline and Nicolet systems were reduced using both discrete Fourier transform and correlation analyses. For the energy spectra analysis, the Nicolet system collected 250,000 samples at a frequency of 1.0 MHz for 0.25 s. The data were broken into 23 blocks and reduced using the discrete Fourier transform (DFT) given by

$$V(f) = \frac{1}{N} \sum_{N} V(t) \exp[-(2\pi i f t/N)] \tag{1}$$

where N is the number of samples, which for the present study was 10,869. The results of the DFT process for each of the 23 blocks were averaged. For each measurement location, two sets of data were acquired, analyzed, and averaged.

The normal-film Eulerian autocorrelation coefficient, $R_E(\tau)$ (Ref. 18) was computed for each block as

$$R_E(\tau) = \left[\frac{(\rho u)'(t)(\rho u)'(t+\tau)}{\overline{(\rho u)'^2}} \right]^2 \tag{2}$$

where the results for each of the 23 blocks were averaged. As with the spectral data, two sets of data were acquired, analyzed, and averaged at each measurement location. The integral timescale Λ was computed from the normalized autocorrelated normal-film data by integrating the area under the autocorrelation function from τ equal to zero to infinity.[19]

The parallel-film probe was also used to collect high-frequency boundary-layer information. The Nicolet data system was used to

collect 128,000 samples from each of the two, parallel, hot-film sensors at a 1.0-MHz rate. The cross-correlation coefficient between the two sensors on the probe was computed using

$$R_E(\tau) = \left\{ \frac{[(\rho u)'(t)]_1 [(\rho u)'(t+\tau)]_2}{\overline{(\rho u)'^2}} \right\}^2 \tag{3}$$

The cross-correlation acquisition and averaging scheme was the same as that used for the single-film probe.

The structure angle associated with a large-scale motion was determined from the time delay between signals for the maximum cross correlation τ, the convection velocity u_c, and the wire separation distance w using the following equation[20]:

$$\theta = \tan^{-1}(w/u_c\tau) \tag{4}$$

The convection velocity was taken here to be the mean flow velocity at the boundary-layer location, which is consistent with the data of Spina et al.[20]

Uncertainty, Noise, and Resolution Estimates

Latin and Bowersox[11] present a description of the uncertainties for the mean and statistical turbulent flow properties listed in Table 1. The uncertainties for the spectral and correlation measurements, which are the focus of this paper, were estimated as described by Bendat and Piersol[18]; the normalized uncertainties were estimated at 8.0%.

The noise floor for the spectral data was estimated as approximately $6.0 \times 10^{-6}/\overline{V'^2}(f)$, accounting for both instrumentation noise, as specified by the manufacturer, and the 12-bit digitization. With this model, a 10% noise level occurred for $\overline{V'^2}(f) \approx 6.0 \times 10^{-5}$. Hence, the present instrumentation allowed for resolution of about three decades of energy drop off, which corresponded to wave numbers less than approximately 600 m^{-1}. The microscales were estimated for the present flowfields with the laser Doppler velocimetry data of Latin and Bowersox[11] and the isotropic relations[21]; the values were nominally in the range of 1.3–2.1 mm, depending on surface condition and location within the boundary layer. Therefore, the wave number range required for microscales resolution was nominally 2900–4800 m^{-1}. Thus, the present analyses were limited to the large-scale motions.

Results and Discussion

Latin and Bowersox[11] demonstrated that the equivalent sand-grain height k_s, as defined by Schlichting,[1] was a useful concept to generalize the effects of roughness on the mean and turbulent statistical flow properties across the boundary layer for the present wind-tunnel models. However, significant topology influences were discerned and discussed. The method of presentation here is to discuss the results in terms of k_s, and the topology effects are described when apparent.

Power Spectra

The normal-film probe was used to collect the frequency-resolved spectra at three locations within the boundary layers ($y/\delta_M = 0.25$, 0.50, and 0.75), at $x = 54.0$ cm, for all six wind-tunnel models. As mentioned in the "Instrumentation" section, these data points were all in the fully turbulent region of the boundary layer. The frequency-resolved measurements provide information on the distribution of turbulent mass-flux power over a range of frequencies from 1.0 kHz to the noise level, which occurred at approximately 40–50 kHz.

Shown in Fig. 3 are the power spectra traces for each of the six models at all three boundary-layer locations. Noticeable in all of the spectra are relatively small spikes in the data, the largest of which is located at ~30 kHz ($k_1 \sim 500$ m^{-1}). This frequency corresponds to a Strouhal (see Ref. 22) number based on the probe holder diameter of approximately 0.22. Hence, these spikes were most likely the result of von Kármán vortex-sheet-induced probe vibrations. Because the effects were highly localized in the frequency domain and the magnitudes were relatively small, the spikes had minimal impact on the subsequent discussions.

An examination of the data in Fig. 3 indicated that the rough-wall energy levels relative to the smooth-plate values increased with

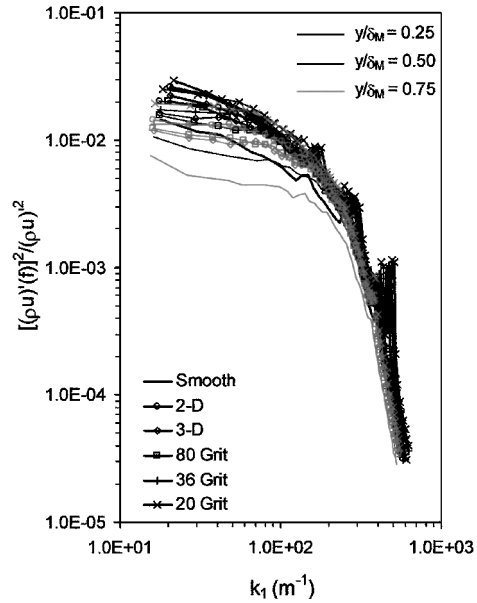

Fig. 3 Power spectra results.

increasing roughness height across the boundary layer. To provide more detail into the relative effects of surface roughness on the low-frequency power spectra [<10 kHz ($k_1 \sim 100$ m^{-1})], a new parameter was defined to be equal to the difference between the rough- and smooth-wall turbulence intensity spectra, normalized by the local turbulence intensity, that is,

$$\Delta_{\rho u(f)\text{rms}} = \left[\sqrt{\frac{\overline{(\rho u)'^2}(f)}{\overline{(\rho u)'^2}}} \right]_{\text{rough}} - \left[\sqrt{\frac{\overline{(\rho u)'^2}(f)}{\overline{(\rho u)'^2}}} \right]_{\text{smooth}} \tag{5}$$

The resulting data, for frequencies of 977–9770 Hz, are plotted vs k_s^+ in Fig. 4 for all three boundary-layer locations. The data in Fig. 4 clearly show the influence of roughness height on the energy increases as a function of frequency and boundary-layer location. Focus first on $y/\delta_M = 0.25$: The energy increases for a given roughness height were bounded on the lower and upper sides by the high-frequency [9770 Hz (dashes)] and low-frequency [977 Hz (squares)] data, respectively. The slope of the increase with roughness height decreased with increasing frequency. Hence, the $y/\delta_M = 0.25$ lines of constant frequency (Fig. 4) fanned out as k_s^+ increased. At $y/\delta_M = 0.50$ and 0.75, the trends were similar, except that the higher frequency rate of increase with roughness increased with increasing boundary-layer height location. Hence, the net effect was that, moving away from the wall, increasing the roughness evened out the energy levels across this frequency range.

A relatively strong topology effect is also noticeable in Fig. 4. The effect is most apparent at $y/\delta_M = 0.75$; however, the trend is noticeable at all three locations. Specifically, if a curve were fit to the sand paper results, the differences between the two- and three-dimensional plates would exceed that predicted by the correlation. If frequency is hypothetically taken to correspond to eddy structure size, that is, a qualitative application of Taylor's hypothesis (see Ref. 19), then this result indicates that the frequency spectrum, and hence the structure size distribution, across the boundary layer depends on the roughness topology. This result is consistent with the statistical properties described by Latin and Bowersox[11] and the incompressible structural data of Grass.[10]

The power spectral results for all six surfaces with inner scaling[7] are shown in Fig. 5 for all three boundary-layer height locations. For the present supersonic measurements, the mass-flux power was scaled by $(\rho_w u^*)^2$. The spectra in Fig. 5 were observed to shift up and to the right with roughness height, where the magnitude of the shifts increased with increasing height within the boundary layer, which signified that surface roughness had a strong impact on the production and transport of turbulent energy across the entire boundary layer. This result is in contrast with the low-speed data of

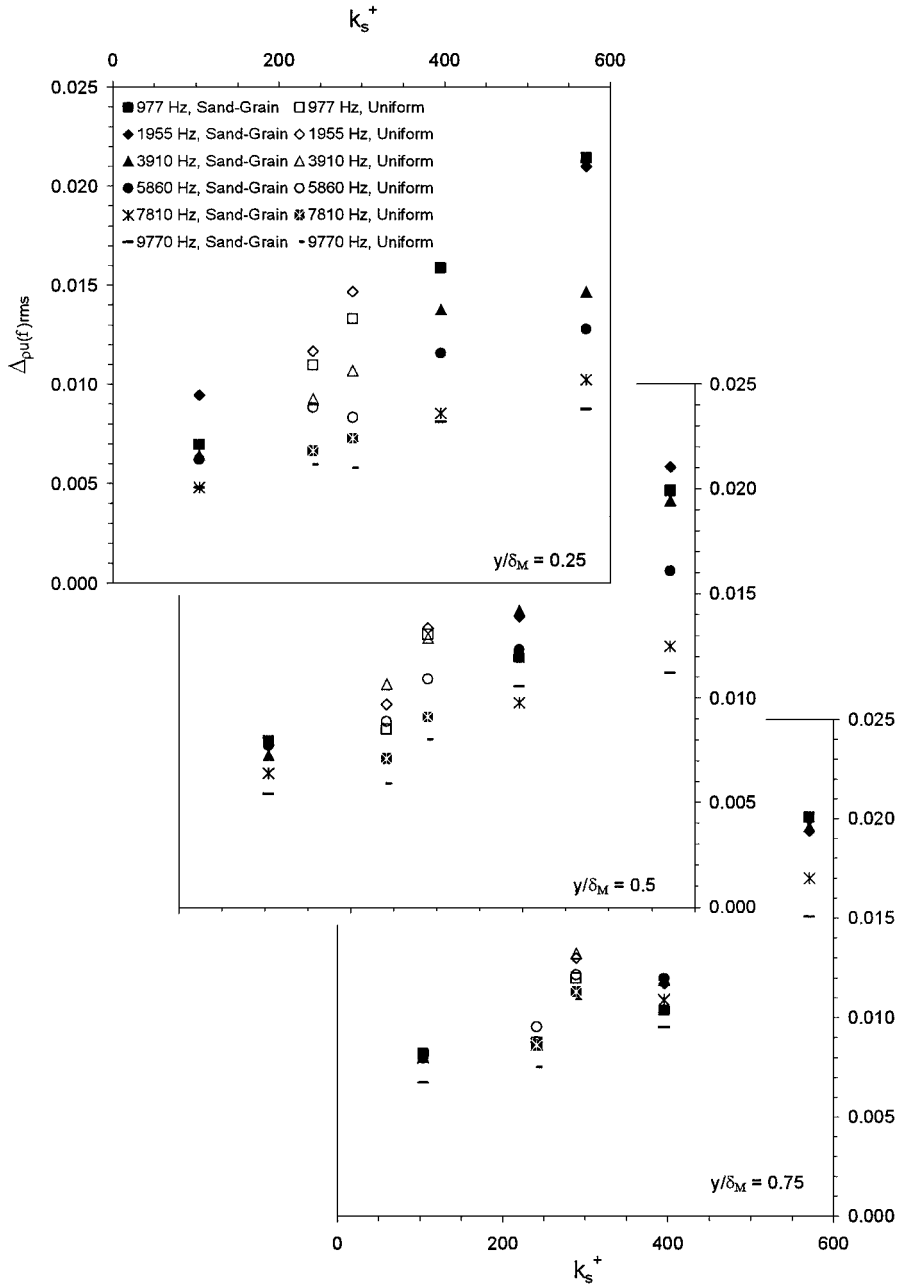

Fig. 4 Power spectra difference vs roughness Reynolds number.

Perry et al.,[7] where the inner-scaling rough-wall data were similar in magnitude (perhaps even lower) in the low-frequency domain. However, their data indicated that the low-frequency energy levels had a Reynolds number dependence, that is, δ^+. Specifically, as δ^+ decreased from 7000 to 500, the low-frequency energy levels increased for both smooth and rough walls. The present data show the opposite trend, and the δ^+ range is narrower (2000–5000) here. Hence, it is unlikely that the trend noticed in Fig. 5 is related to the Reynolds number. Instead, the data in Fig. 5 include important compressibility effects. First, the scaling in Fig. 5 is not identical to that of Perry et al.[7] because in high-speed flow, hot-film anemometry responds to mass-flux fluctuations, that is, density fluctuation information is included. Second, as discussed in the "Introduction," the roughness elements extended beyond the sonic line within the boundary layer, and the associated shock and expansion waves extended into the freestream. These waves introduce a connection between the inner and outer regions of the boundary layer that is not present in low-speed flow and, hence, have the potential to significantly alter the turbulent flow structure.

The turbulent shear stress transport equations for the mass-weighted time-averaged Navier–Stokes equations are given by

$$\tau^T_{ij,t} + \left(\bar{u}_j \tau^T_{ij}\right)_{,j} = -\tau^T_{ik}\bar{u}_{j,k} - \tau^T_{jk}\bar{u}_{i,k} + \overline{u''_j}\bar{p}_{,i} + \overline{u''_i}\bar{p}_{,j} - \bar{\tau}_{ik,k}\overline{u''_j} - \bar{\tau}_{jk,k}\overline{u''_i} - \overline{p'(u''_{i,j} + u''_{j,i})} - [\overline{(\rho u''_i u''_j u''_k)} - \overline{p'u''_i}\delta_{jk} - \overline{p'u''_j}\delta_{ik} + \overline{(\tau'_{ik}u''_j + \tau'_{jk}u''_i)}]_{,k} + \overline{\tau'_{ik}u''_{j,k} + \tau'_{jk}u''_{i,k}} \quad (6)$$

The form of Eq. (6) is similar to that reported in Wilcox.[2] The only difference is that the viscous-work terms [fifth and sixth terms on the right-hand side of Eq. (6)] have been separated out of the dissipation here. Otherwise, the term-by-term enumeration of Eq. (6) is given by Wilcox. The roughness-element-generated shock and expansion waves that traverse the boundary layer result in locally large kinematic and thermodynamic mean flow gradients that directly alter, that is, explicit dependence, the convection [second term on the left-hand-side of Eq. (6)], the production (first two terms on the right-hand side), the pressure work (third and fourth terms on the right-hand side) and the viscous work (fifth and sixth terms on the

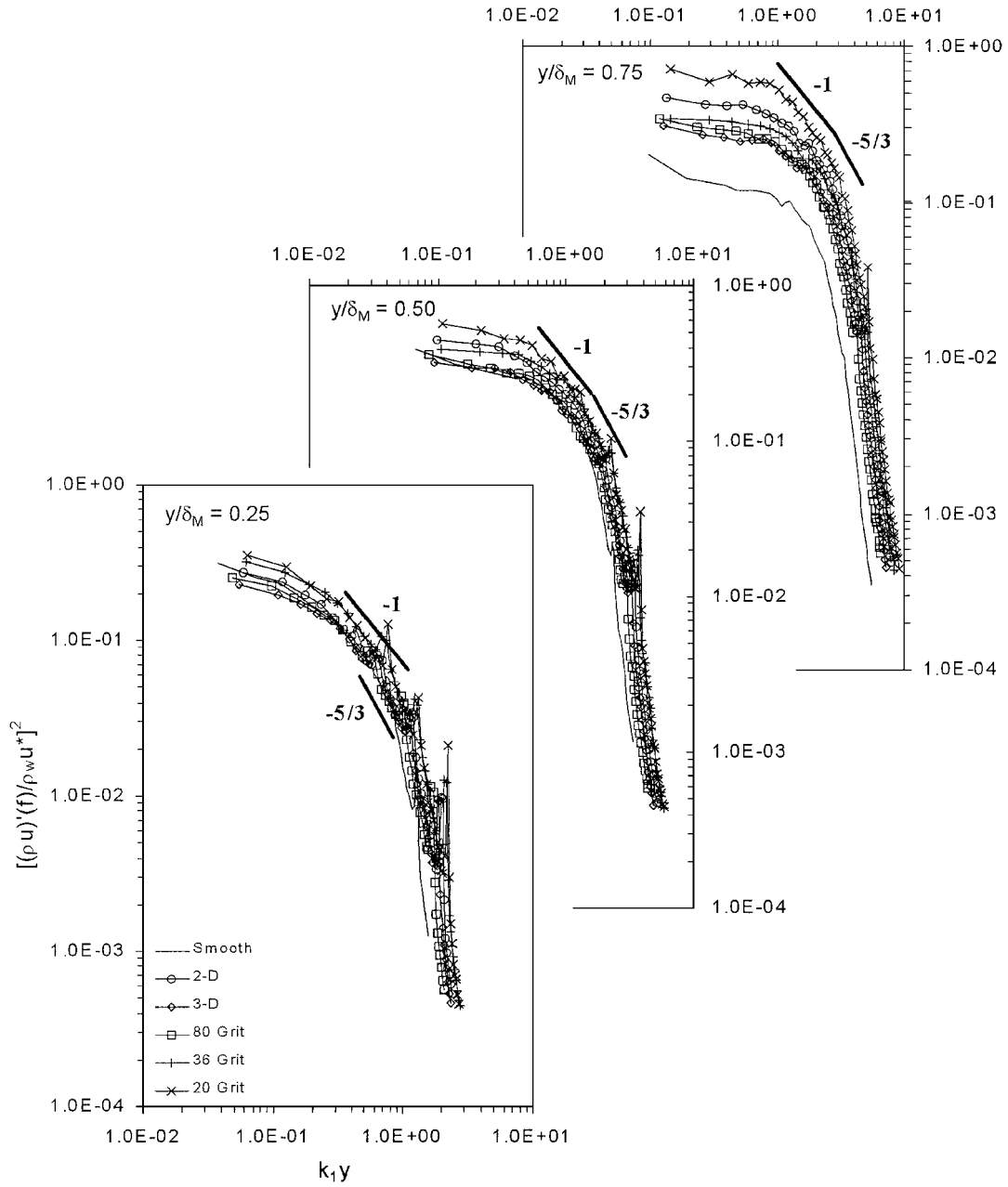

Fig. 5 Energy spectra results with inner scaling.

right-hand side) as compared to low-speed flow. In addition, the data of Latin and Bowersox[11] demonstrated that the fluctuation properties with thermodynamic dependence, for example, $\overline{\rho' v'}$, were strongly amplified by the wall roughness. A plausible explanation for this amplification was the interaction of the waves with the boundary-layer turbulence. The increased thermodynamic fluctuations have a direct impact (explicit dependence) on the pressure-work, pressure-strain redistribution (seventh term on the right-hand side) and turbulence-diffusion (eighth term on the right-hand side). This new transport mechanism (shock and expansion waves) depend explicitly on the roughness height and geometry.

Both overlap regions, as indicated by the -1 and $-\frac{5}{3}$ slopes (annotated in Fig. 5), were present in the all of the $y/\delta_M = 0.25$ and 0.5 rough-wall spectral traces. The smooth-wall data agree qualitatively well with that described by Smits and Dussuage.[23] However, because the Reynolds numbers were significantly lower in the present study, the range of wave numbers for the second overlap region was smaller in the present study as compared to that shown by Smits and Dussuage. This Reynolds number dependency for low-speed smooth and rough walls is described by Raupach et al.[6] At $y/\delta_M = 0.75$, the rough-wall data show the overlap regions, and the smooth-wall trace does not. For the smooth plate at $y/\delta_M = 0.75$, the absence of the overlap regions and the relatively large decrease in energy as compared to the nearer wall measurements agrees with the incompressible results of Perry et al.[7] Thus, although the production mechanism[6] was altered by the combination of roughness and compressibility, the expected energy cascade and dissipation appeared to be present.

To test the usual compressibility scaling, the spectral results were also converted into velocity fluctuations using the strong Reynolds analogy[23] and scaled for compressibility.[24,25] The velocity and mass-flux spectra with outer scaling for the smooth and 20-grit plate are compared in Fig. 6. The 20-grit velocity fluctuation data with outer scaling was found to collapse at all three boundary-layer locations except at low frequencies ($k_1\delta < 0.7$). The smooth-plate velocity fluctuation data did not scale as well, where at $y/\delta_M = 0.75$ the data fell significantly below the $y/\delta_M = 0.25$ and 0.5 traces. This downward shift is consistent with the incompressible data of Perry et al.[7] The outer variable mass-flux scaling did not collapse the data as well. The results for the intermediate roughness heights demonstrated similar scaling trends.

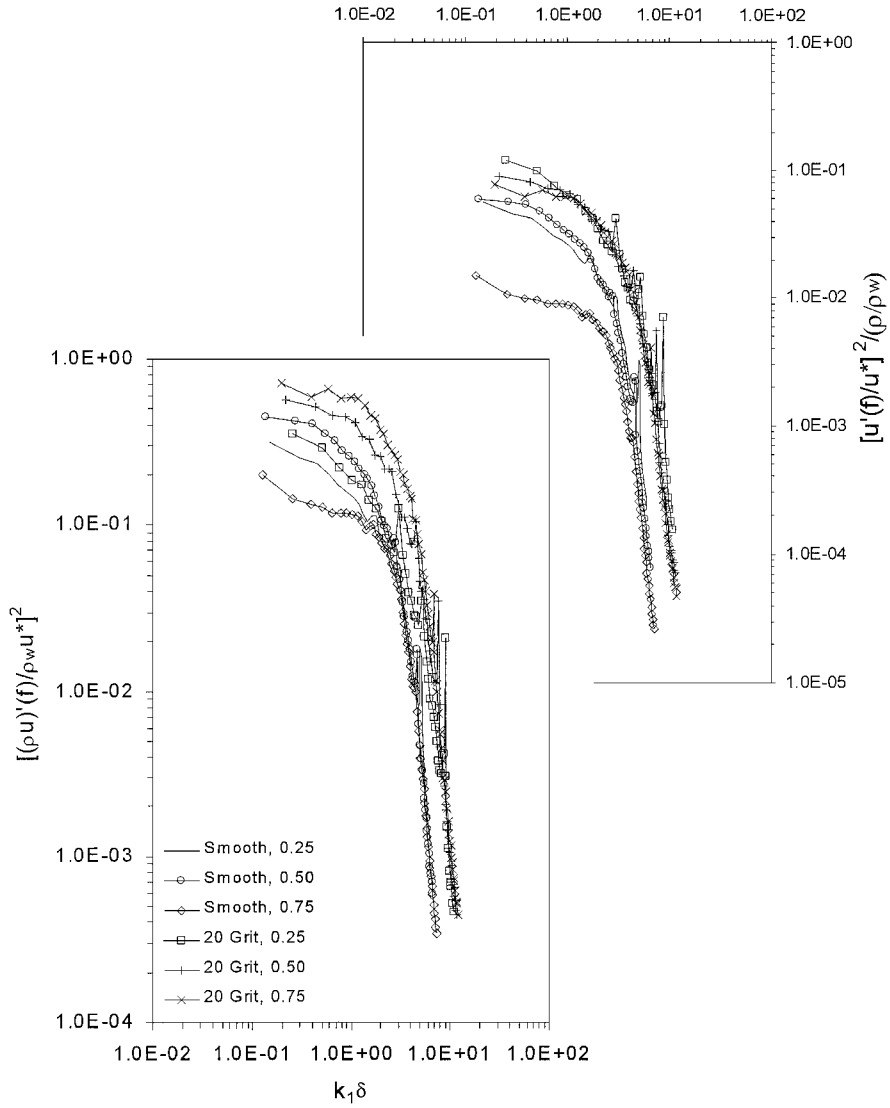

Fig. 6 Energy spectra results with outer scaling.

Autocorrelation and Integral Scales

Autocorrelation information was calculated from the normal-film probe time history data; example correlation data ($y/\delta_M = 0.25$) are presented in Fig. 7. All of the traces reached zero, to within the expected level of noise [$\sim$0.04 in $R_E(\tau)$], near $\tau = 100$–200 μs. This range of τ depended on the roughness and boundary-layer location. The plot in Fig. 7 was limited to 50 μs to better show the details of the trace. For $\tau < 35$ μs, the correlation traces are bounded by the smooth plate on the lower side and the 20-grit and two-dimensional plates on the upper side. The faster decrease for the smooth plate indicates smaller small-scale structures in a temporal sense. Hence, the traces in Fig. 7 indicated that the small-scale structure size increased with increasing roughness. However, the for $\tau > 35$ μs, the smooth-plate trace begins to level off and cross over the rough-wall plates, which indicated that the large-scale structures were largest for the smooth plate. The trends at $y/\delta_M = 0.5$ and 0.75 are similar to those discussed earlier.

To quantify better how surface roughness affected the large-scale flow structure sizes, the integral-timescale values for each model were calculated[19] and are shown Fig. 8. Typically, Taylor's hypothesis (see Ref. 19) is used to present autocorrelation structure timescales as length scales; however, this only works well for low-turbulence levels ($<1\%$) (Ref. 19). For this reason, the timescales are presented. However, qualitative inference to the structure dimension was inferred from the temporal scales. The data in Fig. 8 indicate that the integral timescales decreased as the wall was approached from the freestream, which is consistent with the idea

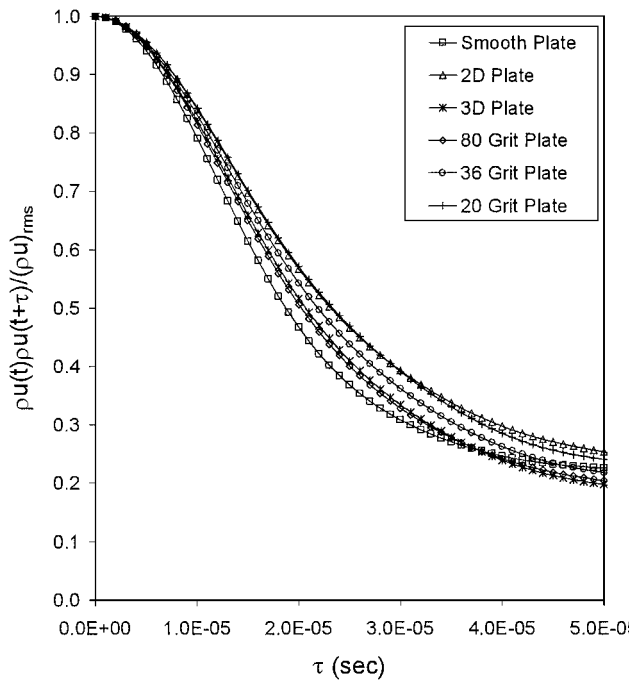

Fig. 7 Example autocorrelation functions.

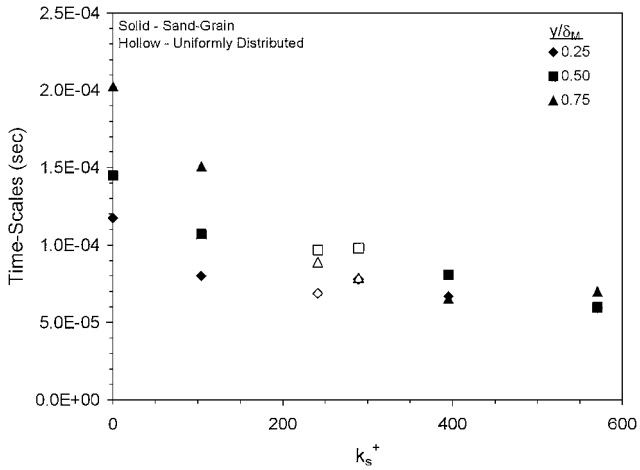

Fig. 8 Integral timescales.

that the wall dampens or limits the large-scale structure sizes. Surface roughness was also found to decrease the magnitude of the integral length scale in all three boundary-layer regions. The rate of decrease of the integral scale with roughness increased with increasing y/δ_M, and the integral scale was found to be nominally independent of the location within the boundary layer for the larger roughness heights (specifically, for k_s^+ greater than about 250).

When the machined-plate results (open symbols in Fig. 8) were compared to sand-grain-plate results, it was clear that the equivalent sand-grain height was effective in capturing the overall trends; however, topology dependences were discernable. In other words, the machined-plate results were near the sand-paper plate trends; however, the differences between the three-dimensional and two-dimensional plate were systematic. Specifically, the two-dimensional plate $y/\delta_M = 0.25$ integral scale was also much higher than would be indicated by the sand-grain plate results. The two-dimensional plate produced a cavity-type flow that shed structures that were strongly correlated in the x direction,[11] thus explaining this observation.

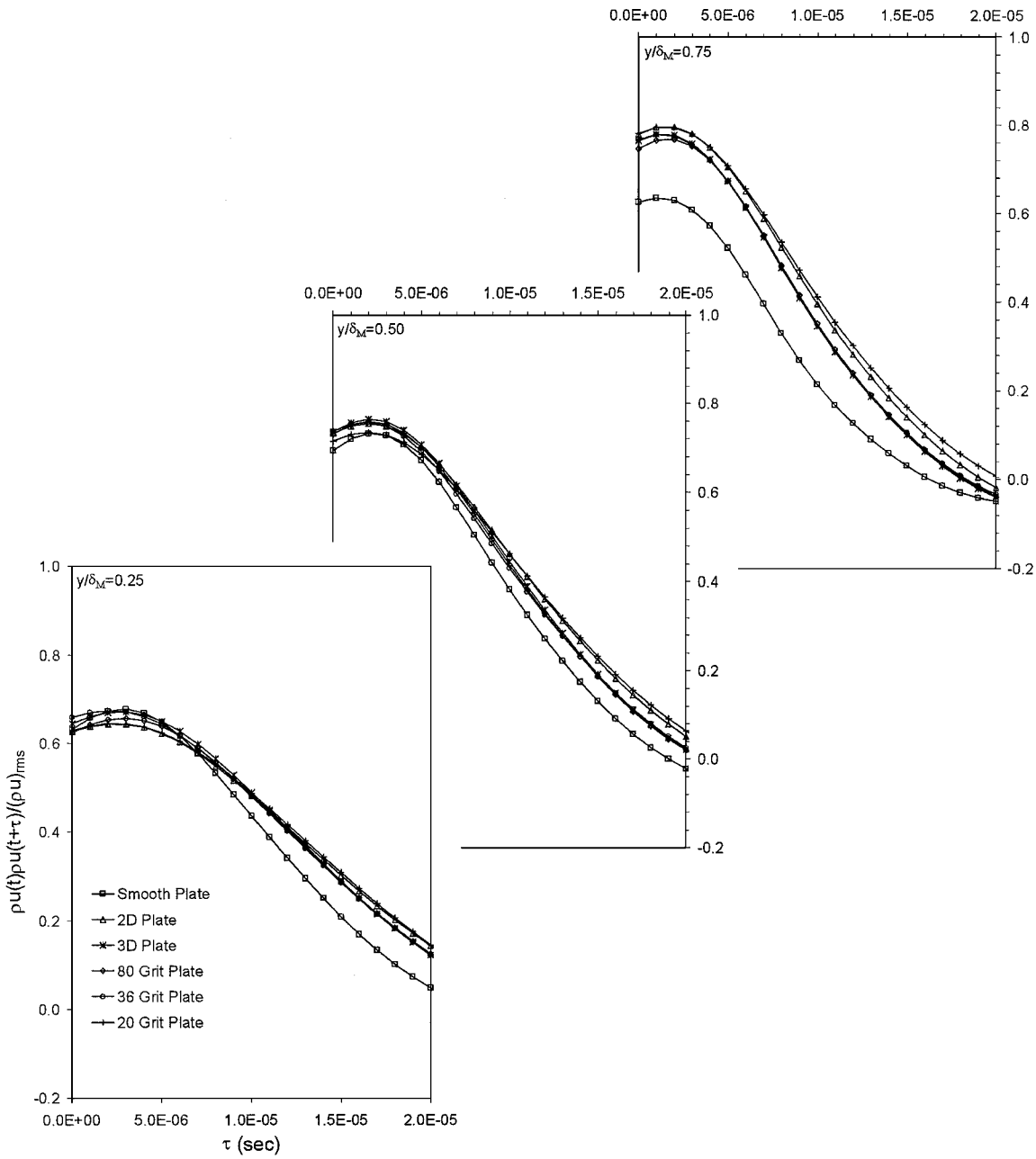

Fig. 9 Parallel-wire cross-correlation traces.

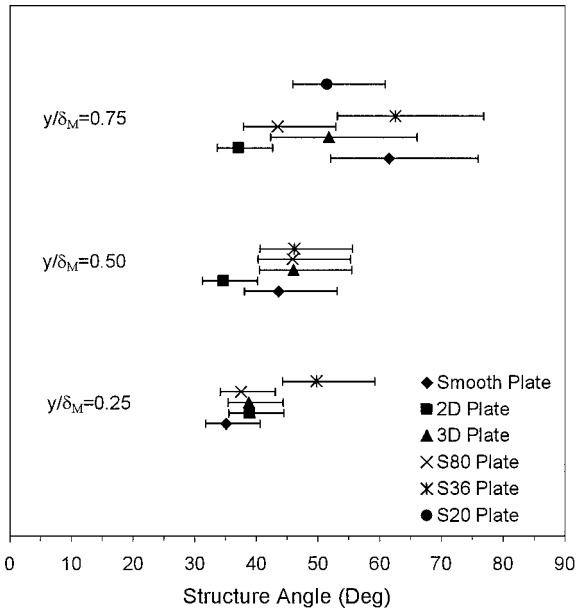

Fig. 10 Structure angle.

Cross Correlation

Presented in Fig. 9 are the cross-correlation time traces for each of the three boundary-layer height locations for all six plates. For all six models, the cross-correlation dropoff rate is largest at $y/\delta_M = 0.75$, followed by $y/\delta_M = 0.50$, and then $y/\delta_M = 0.25$. When it is assumed that x–y planar cuts of the eddies are elliptical and that the mean streamwise velocity of the eddies is significantly faster than the eddy rotational velocity, the drop off rate gives an indication of the eddy streamwise thickness for eddies with a height of at least the parallel-film sensor separation distance. The dropoff rate shows that the smaller scale eddy streamwise thickness was largest near the wall boundary and decreased moving toward the freestream. This result from the parallel-film cross correlation agreed with the autocorrelation results. The drop off rate was found to decrease with increasing k_s, indicating qualitatively that surface roughness increased the smaller scale streamwise thickness. These results also agreed with the normal-film autocorrelation results.

The flow structure angles estimated from the cross-correlation traces [Eq. (4)] are shown in Fig. 10 along with uncertainty bars indicating sampling rate resolution. The smooth-plate result increased from 35 to 60 deg as y/δ_M increased from 0.25 to 0.75, which was in excellent agreement with the Spina et al.[20] results. It appears that, with the exception of the two-dimensional plate and to within the measurement uncertainty, the smooth-plate trend holds for the rough-wall models. Unlike the other plates, the two-dimensional plate flow structure angles remained relatively constant across the boundary layer at a value of approximately 35 deg.

Conclusions

An experimental investigation examining the influence of surface roughness on the temporal turbulent flow structure of a supersonic, high-Reynolds-number ($M = 2.9$, $Re/m = 1.9 \times 10^7$) boundary layer was performed. Normal- and parallel-film anemometry was used to survey the boundary layers at three locations ($y/\delta_M = 0.25$, 0.5, and 0.75) for six different wall topologies ($k_s^+ = 0$–571). In general, the results of this study describe the influence of surface roughness height and topology on the large-scale temporal structure in the fully turbulent region of the boundary layer. A list of specific results follows:

1) The spectral data indicated that the rough-wall energy levels across the boundary layer relative to the smooth plate increased with increasing roughness height. 2) For frequencies in the range of 0.98–9.8 kHz, the energy level increases with increasing roughness became more uniform across the frequency spectrum. 3) When plotted with inner variable scaling, the spectral traces at all three boundary-layer locations were found to shift up and to the right, and the shifts increased with increasing roughness height. 4) Both overlap regions (I and II) were discernible in the smooth- and rough-wall spectral trace with inner scaling. 5) Converting the cross-film mass-flux data to velocity using the strong Reynolds analogy and scaling for compressibility were found to collapse the rough-wall data at the three boundary-layer locations over most of the wave number range, when plotted with outer scaling. 6) The integral timescales were found to decrease by as much as 250% with increasing roughness height and were found to be nominally independent of boundary-layer location ($y/\delta_M = 0.25$–0.75) for k_s^+ greater than approximately 250. 7) The cross-correlation data showed that the streamwise thickness of the turbulence structures decreased with increasing roughness height. 8) The large-scale structure angles across the boundary layer for the sand-grain and three-dimensional plates were similar to the smooth-plate values; however, the two-dimensional plate structures were at nominally constant angle of 35 deg. Last, specific topology effects were discerned and discussed.

In summary, all of the quantitative data presented herein indicated that roughness had the effect of populating the supersonic boundary layers with higher energy eddies, that is, fluctuating levels, that were distributed over a narrower range of scales, as compared to the smooth plate. The roughness elements had the effect of altering the turbulence production and transport mechanisms across the entire boundary layer, as compared to the smooth plate, and a direct connection (roughness-generated shocks and expansion waves) between the inner and outer layers was discussed. In addition, the presence of the overlap regions indicated that the expected energy cascade and dissipation mechanisms[7,19,23] were present for the supersonic rough-wall boundary-layer flows. Last, the noticeable topology effects further signify the connection between the inner and outer region of the supersonic rough-wall boundary layers.

Acknowledgments

The authors gratefully acknowledge Mark Glauser and Thomas Beutner of the U.S. Air Force Office of Scientific Research and Diana Glawe and Mark Gruber of the U.S. Air Force Research Laboratory, Propulsion Directorate, for sponsoring this work.

References

[1]Schlichting, H., *Boundary Layer Theory*, 7th ed., McGraw–Hill, New York, 1979, pp. 489–728.

[2]Wilcox, D., *Turbulence Modeling for CFD*, DCW Industries, Inc., La Cañada, CA, 1993, pp. 1–22, 171–210.

[3]Fernholz, I., Finley, M., and Mikulla, V., "A Futher Compilation of Compressible Boundary Layer Data with a Survey of Turbulence Data," AGARDograph 263, NATO, Technical Editing and Reproduction, Ltd., London, Nov. 1981.

[4]Nikuradse, J., "Stromungsgesetze in Rauhen Rohren," *Forschung Arb. Ingenieurwesen*, No. 361, 1933.

[5]Antonia, R. A., and Wood, D. H., "Calculation of a Turbulent Boundary Layer Downstream of a Small Step Change in Surface Roughness," *Aeronautical Quarterly*, Vol. 26, Aug. 1975, pp. 202–210.

[6]Raupach, M., Antonia, R., and Rajagopalan, S., "Rough Wall Turbulent Boundary Layers," *Applied Mechanics Reviews*, Vol. 44, Jan. 1991, pp. 1–25.

[7]Perry, A. E., Lim, K. L., and Henbest, S. M., "An Experimental Study of the Turbulence Structure in Smooth and Rough Wall Boundary Layers," *Journal of Fluid Mechanics*, Vol. 177, 1987, pp. 437–466.

[8]Townsend, A. A., *The Structure of Turbulent Shear Flow*, 2nd ed., Cambridge Univ. Press, Cambridge, England, U.K., 1976.

[9]Kolmogorov, A. N., "Local Structure of Turbulence in Incompressible Viscous Fluid for Very Large Reynolds Number," *Comptes Rendus (Doklady) de l'Academie des Sciences de l'URSS*, Vol. 30, No. 4, 1941, pp. 301–305.

[10]Grass, A., "Structural Feature of Turbulent Flow over Smooth and Rough Boundaries," *Journal of Fluid Mechanics*, Vol. 50, Pt. 2, 1971, pp. 233–255.

[11]Latin, R., and Bowersox, R., "Flow Properties of a Supersonic Boundary Layer with Wall Roughness," *AIAA Journal*, Vol. 38, No. 10, 2000, pp. 1804–1821.

[12]Goddard, F., "Effects of Uniformly Distributed Roughness on Turbulent Skin-Friction Drag at Supersonic Speeds," *Journal of the Aero/Space Sciences*, Vol. 26, No. 1, 1959, pp. 1–24.

[13]Berg, D., "Surface Roughness Effect on a Mach 6 Turbulent Boundary Layer," *AIAA Journal*, Vol. 17, No. 9, 1979, pp. 929, 930.

[14]Reda, D., Ketter, F., and Fan, C., "Compressible Turbulent Skin Friction on Rough and Rough/Wavy Walls in Adiabatic Flow," *AIAA Journal*, Vol. 13, No. 5, 1975, pp. 553–555.

[15]Dussuage, J.-P., Smith, R., Smits, A., Fernholtz, H., Finley, P., and Spina, E., "Turbulent Boundary Layers in Subsonic and Supersonic Flow," AGARDograph 335, NATO, Canada Communications Group, Hull (Quebec), Canada, July 1996.

[16]Latin, R. M., "The Influence of Surface Roughness on Supersonic High Reynolds Number Turbulent Boundary Layer Flow," Ph.D. Dissertation, AFIT/DS/ENY/98M-02, Air Force Inst. of Technology, Wright–Patterson AFB, OH, April 1998.

[17]Luker, J. J., Bowersox, R., and Buter, T., "Influence of a Curvature Driven Favorable Pressure Gradient on a Supersonic Turbulent Boundary Layer," *AIAA Journal*, Vol. 38, No. 8, 2000, pp. 1351–1359.

[18]Bendat, J., and Piersol, A., *Random Data Analysis and Measurement Procedures*, 2nd ed., Wiley, New York, 1986, pp. 252–322.

[19]Cebeci, T., and Smith, A. M. O., *Analysis of Turbulent Boundary Layers*, Applied Mathematics and Mechanics, Academic Press, New York, 1974, pp. 15–22.

[20]Spina, E., Donovan, J., and Smits, A., "On the Structure of High-Reynolds Number Supersonic Turbulent Boundary Layers," *Journal of Fluid Mechanics*, Vol. 222, Jan. 1991, pp. 293–327.

[21]Hinze, *Turbulence*, McGraw–Hill, New York, 1975, pp. 175–315.

[22]White, F., *Fluid Mechanics*, 3rd ed., McGraw–Hill, New York, 1994, pp. 269, 270.

[23]Smits, A., and Dussuage, J.-P., *Turbulent Shear Layers in Supersonic Flow*, American Inst. of Physics, Woodbury, New York, 1996, pp. 197–252.

[24]Morkovin, M., "Effects of Compressibility on Turbulent Flows," *The Mechanics of Turbulence*, edited by A. Favre, Gordon and Breach, New York, 1961, pp. 368–380.

[25]Van Driest, E., "Turbulent Boundary Layers in Compressible Fluids," *Journal of Aeronautical Sciences*, Vol. 26, No. 3, 1951, pp. 287–319.

W. J. Devenport
Associate Editor